Supplementary Information

Development of a wireless bioelectronic actuator for wound healing in a porcine model

Prabhat Baniya[1,*], Maryam Tebyani[1], Wan Shen Hee[1], Houpu Li[1], Narges Asefifeyzabadi[1], Kaelan Schorger[1], Hsin-ya Yang[2], Anthony Gallegos[2], Kan Zhu[2,3], Fan Lu[4], Gordon Keller[1], Celeste Franco[1], Koushik Devarajan[1], Alexie Barbee[1], Cristian Hernandez[1], Tiffany Nguyen[1], Cynthia Recendez[2,3], Elham Aslankoohi[1], Roslyn Rivkah Isseroff[2], Min Zhao[2,3], Marcella Gomez[4], Marco Rolandi[1,*], and Mircea Teodorescu[1,5,*]

[1]Department of Electrical and Computer Engineering, University of California Santa Cruz, Santa Cruz, California, 95064, USA
[2]Department of Dermatology, School of Medicine, University of California Davis, Sacramento, California, 95816, USA
[3]Department of Ophthalmology & Vision Science, University of California Davis, Sacramento, California, 95817, USA
[4]Department of Applied Mathematics, University of California Santa Cruz, Santa Cruz, California, 95064, USA
[5]Genomics Institute, University of California Santa Cruz, Santa Cruz, California, 95060, USA
[*]pbaniya@ucsc.edu, mrolandi@ucsc.edu, mteodore@ucsc.edu

Supplementary figures and text

In vivo experimental procedures and setup

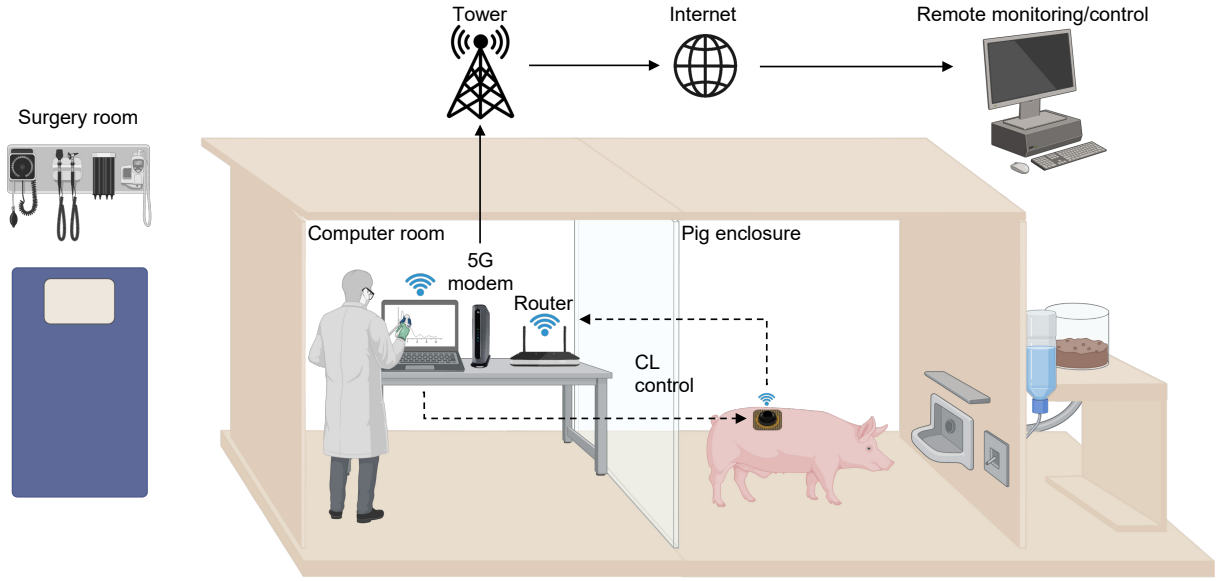

Figure S1. The pig is first anesthetized in a surgery room where wounds are created, and the wireless bioelectronic devices are applied. The pig is then transferred to a nearby enclosure. After that, closed-loop (CL) control of Flx^{+} and/or EF delivery can be initiated, and the device transmits real-time data to the laptop via WiFi in an adjacent room operated by a researcher. The setup also supports remote monitoring and control through 5G internet connectivity, enabling real-time oversight by researchers. The animal has access to water and food, ensuring its welfare during long-term monitoring studies. Created with BioRender.com and annotated in Microsoft PowerPoint 2025.

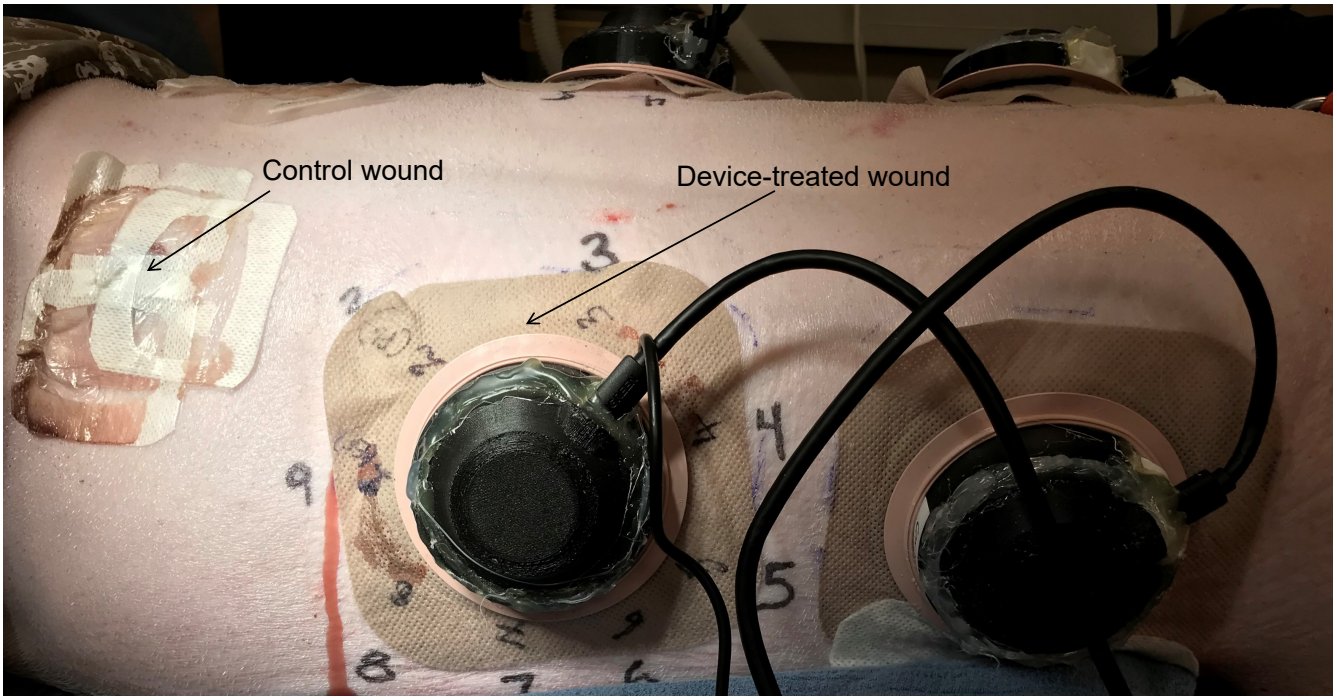

Figure S2. Device-treated and control (standard-of-care) wounds on the back of a pig. Wireless bioelectronic devices are secured to the treated wounds with the help of a skin barrier and tape.

ADC and I-DAC calibration

The ideal (uncalibrated) output code A_i of the ADC at each channel i, or electrode E_i, for an input voltage V_i, or electrode voltage V_{E_i}, is given by

$$A_{i/E_i} = \frac{2^{N_{adc}}}{V_{CC}} V_{i/E_i} \tag{1}$$

Two-point calibration of the ADC offset and gain is performed to enable accurate voltage and current measurements at each channel. Input voltages chosen for calibration are $V_c^1 = 0$ V and $V_c^2 \approx 4.7$ V, which are set by putting the I-DAC in voltage output mode and setting its output to the minimum and maximum, respectively. These values were chosen as calibration points because they fall within the linear range of the ADC. All channels must be left open-circuited during voltage calibration, during which ADC measurements $A_{c_i}^1$ and $A_{c_i}^2$ for the two calibration points are made at each channel i by the device internally. The corresponding voltage measurements $V_{c_i}^1$ and $V_{c_i}^2$ for the two calibration points are made at each channel i externally using a multimeter, as shown in Fig. S3, but without the resistor. The calibrated output code A_{c_i} of the ADC at each channel i is given by

$$A_{c_i} = m_{adc_i} V_{c_i} + b_{adc_i} \tag{2}$$

where

$$m_{adc_i} = \frac{A_{c_i}^2 - A_{c_i}^1}{V_{c_i}^2 - V_{c_i}^1} \tag{3}$$

and

$$b_{adc_i} = A_{c_i}^1 - m_{adc_i} V_{c_i}^1 \tag{4}$$

are the ADC calibration coefficients.

After calibration, the resistor is put back in series at each channel individually, as shown in Fig. S3, and the I-DAC output code is swept from 0 to 255 to vary the ADC input voltage from 0 to 4.7 V. The ideal, calibrated, and measured ADC voltage transfer functions for all channels are shown in Fig. S5.

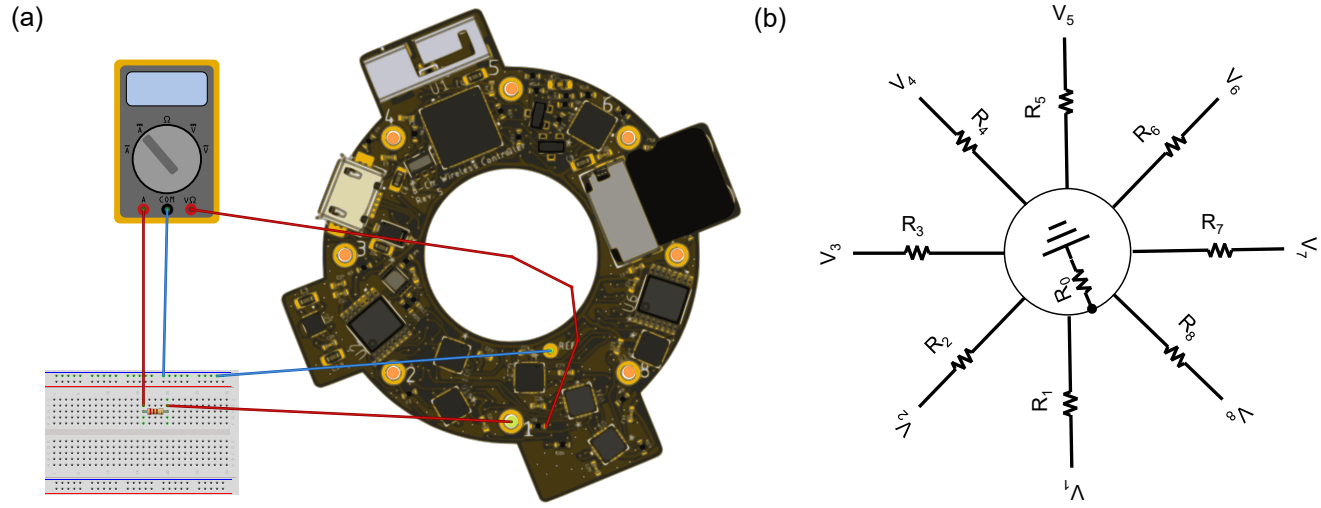

Figure S3. (a) To calibrate the ADCs and DACs, a multimeter and a breadboard are used to measure the current flowing through and the voltage across a 46.13 kΩ resistor at each channel (PTH) of the PCB. (b) A circuit diagram for in-house PCB testing, where each channel is loaded with resistors to emulate a device delivering drugs to the wound.

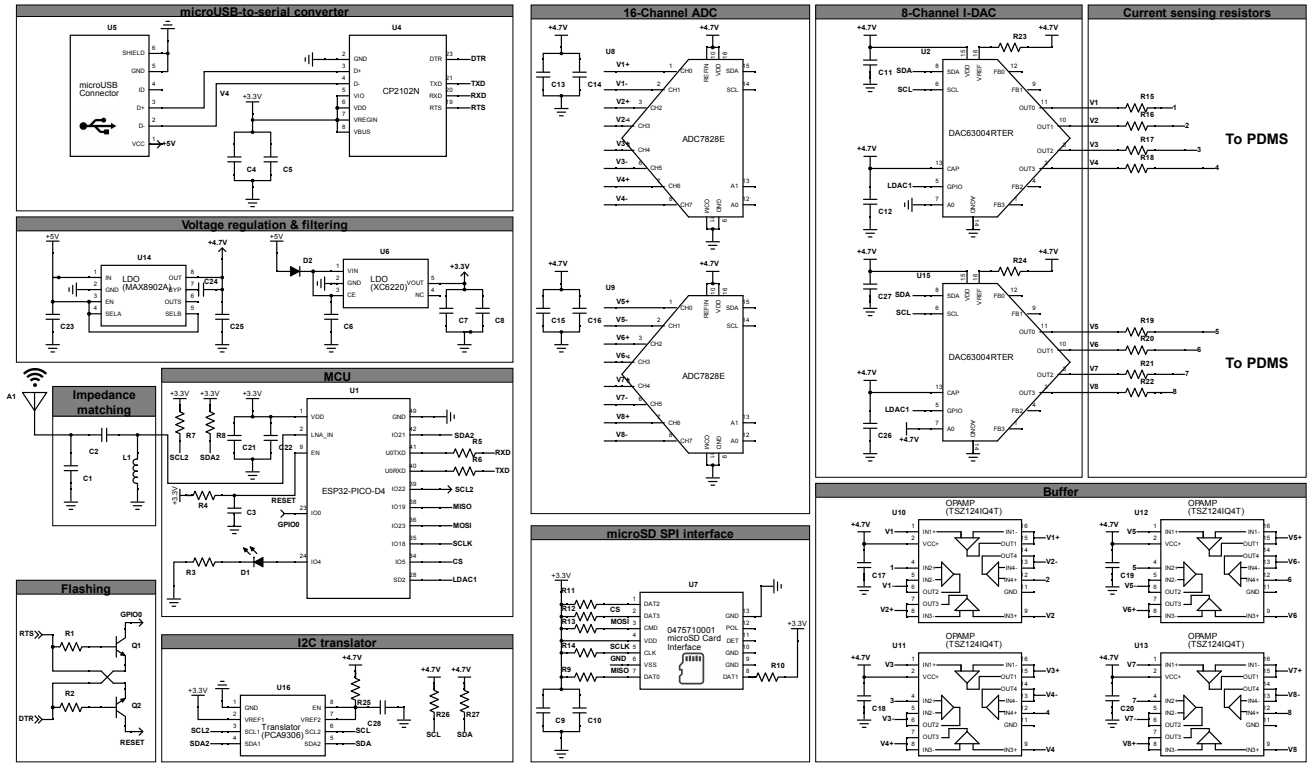

Figure S4. Detailed circuit diagram of wireless bioelectronic actuator PCB showing the interconnection between the MCU, ADCs, I-DACs, opamps, microSD card, USB-to-serial converter, LDO regulators, power supply, flashing circuit, antenna, impedance matching network, SPI, and I^2C interfaces.

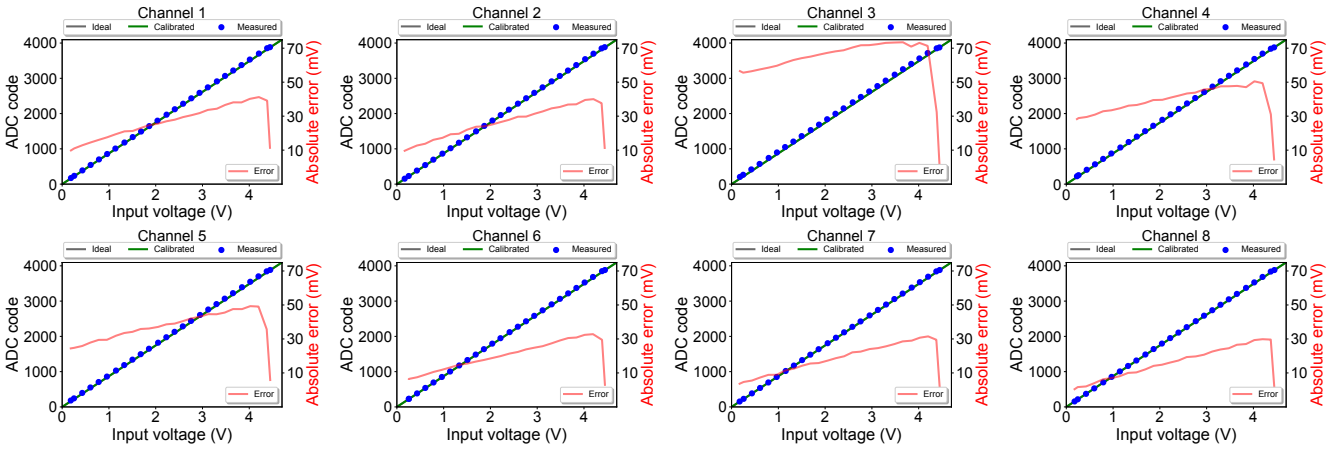

Figure S5. ADC voltage transfer functions and absolute voltage errors for all 8 channels.

The ideal (uncalibrated) output current I_i of the I-DAC at each channel i, for an input code D_i, is given by

$$I_i = \frac{I_{max}}{2^{N_{idac}}} D_i \tag{5}$$

Two-point calibration of the I-DAC offset and gain is performed to enable accurate current measurements at each channel. Nominal currents chosen for calibration are designated as $I_c^1 \approx 2\ \mu$A and $I_c^2 \approx 50\ \mu$A, corresponding to I-DAC codes $D_c^1 = 1$ and $D_c^2 = 255$, respectively. These values were chosen as calibration points because they fall within the linear range of the I-DAC. Each channel has a 46.13 kΩ calibration resistor connected between it and ground (center channel, 0 V) to allow current flow during calibration, during which multimeter measurements $I_{c_i}^1$ and $I_{c_i}^2$ for the two calibration points are made at each channel i. These currents are measured using a multimeter, as shown in Fig. S3. The calibrated output current I_{c_i} of the I-DAC at each channel i is given by

$$I_{c_i} = m_{idac_i} D_i + b_{idac} \tag{6}$$

where

$$m_{idac_i} = \frac{I_{c_i}^2 - I_{c_i}^1}{D_{c_i}^2 - D_{c_i}^1} \tag{7}$$

and

$$b_{idac_i} = I_{c_i}^1 - m_{idac_i} D_{c_i}^1 \tag{8}$$

are the I-DAC calibration coefficients.

The I-DAC output code is swept from 0 to 255 to vary the I-DAC output current from 0 to 50 μA.. The ideal, calibrated, and measured DAC transfer functions for all channels are shown in Fig. S6.

The difference (diff.) of two uncalibrated ADC codes, A_i at channel i and A_{E_i} at electrode i, is related to the input current I_i at channel i, as follows:

$$A_i - A_{E_i} = I_i(\mu\text{A})\, 0.01\, \frac{2^{N_{adc}}}{V_{CC}} \tag{9}$$

where I_i is the input current calculated from uncalibrated input voltages, ranging from 0 to 50 μA (as I-DAC code D_i is varied from 0 to $2^{N_{dac}} - 1$), and is given by

$$I_i(\mu\text{A}) = (V_i - V_{E_i})\, 100 \tag{10}$$

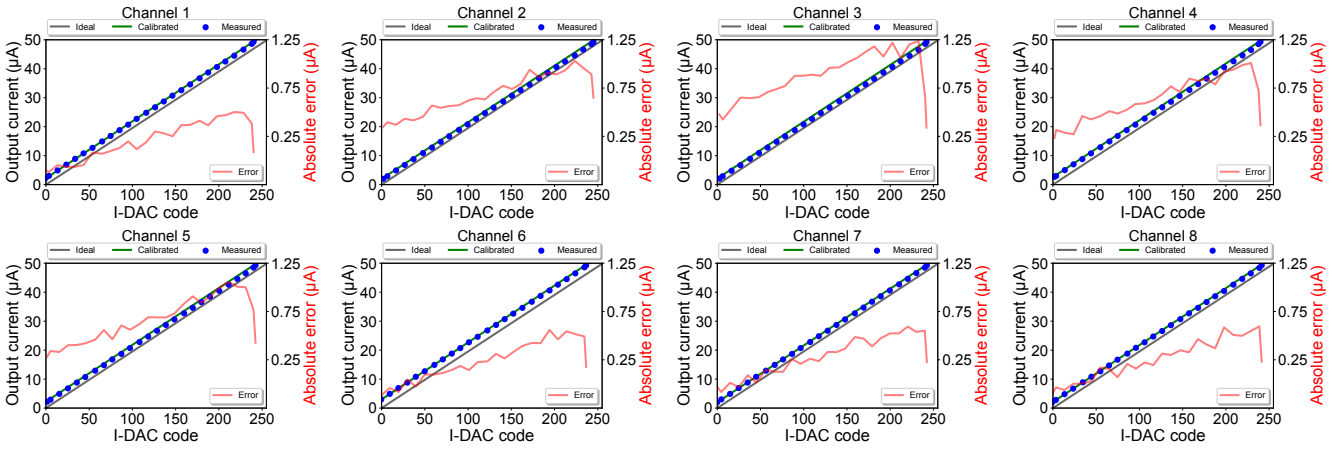

Figure S6. I-DAC current transfer functions and absolute current errors for all 8 channels.

The difference (diff.) of two calibrated ADC codes, A_{c_i} at channel i and $A_{E_{c_i}}$ at electrode i, is related to the current I_i at channel i, as follows:

$$A_{c_i} - A_{E_{c_i}} = I_{c_i}(\mu\text{A})\,0.01\,m_{adc_i} + b_{adc_i} - b_{adc_{E_i}}\frac{m_{adc_i}}{m_{adc_{E_i}}} \tag{11}$$

where I_{c_i} is the input current calculated from calibrated input voltages, ranging from 0 to 50 μA (as the I-DAC code D_i is varied from 0 to $2^{N_{dac}} - 1$), and is given by

$$I_{c_i}(\mu\text{A}) = (V_{c_i} - V_{c_{E_i}})\,100 \tag{12}$$

The I-DAC code is swept from 0 to 255 to vary the ADC input current from 0 to 50 μA. The ideal, calibrated, and measured ADC current transfer functions for all channels are shown in Fig. S7.

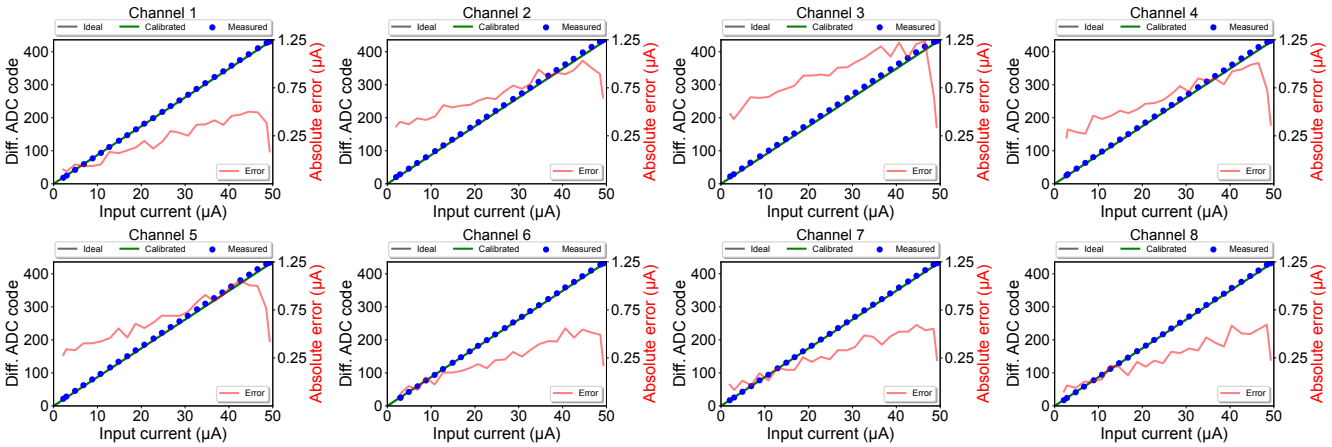

Figure S7. ADC current transfer functions and absolute current errors for all 8 channels.

Graphical user interface (GUI)

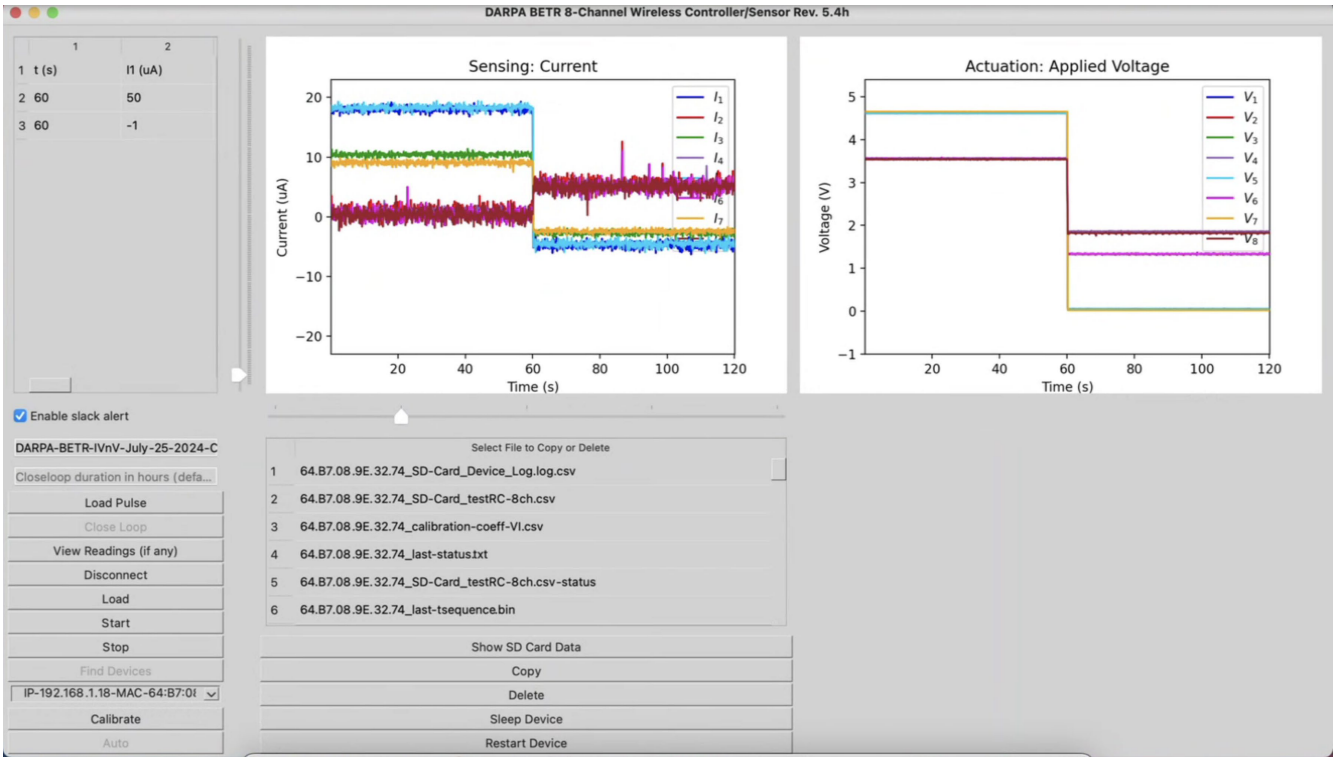

Figure S8. Graphical user interface (GUI) for data acquisition and control of wireless bioelectronic actuators. The GUI supports simultaneous operation of multiple devices.

Antenna

Fig. S9a also shows how the antenna and its 3D radiation pattern are aligned. The pattern is broader, and the gain is higher along the positive x-axis (the right side of the antenna), as evident in the horizontal (xy) plane pattern in Fig. S9b. The vertical plane patterns show that the radiation above (+z-axis) and below (-z-axis) the antenna is approximately the same. The vertical (yz) plane pattern indicates that the gain is higher along the positive y-axis (the front of the antenna).

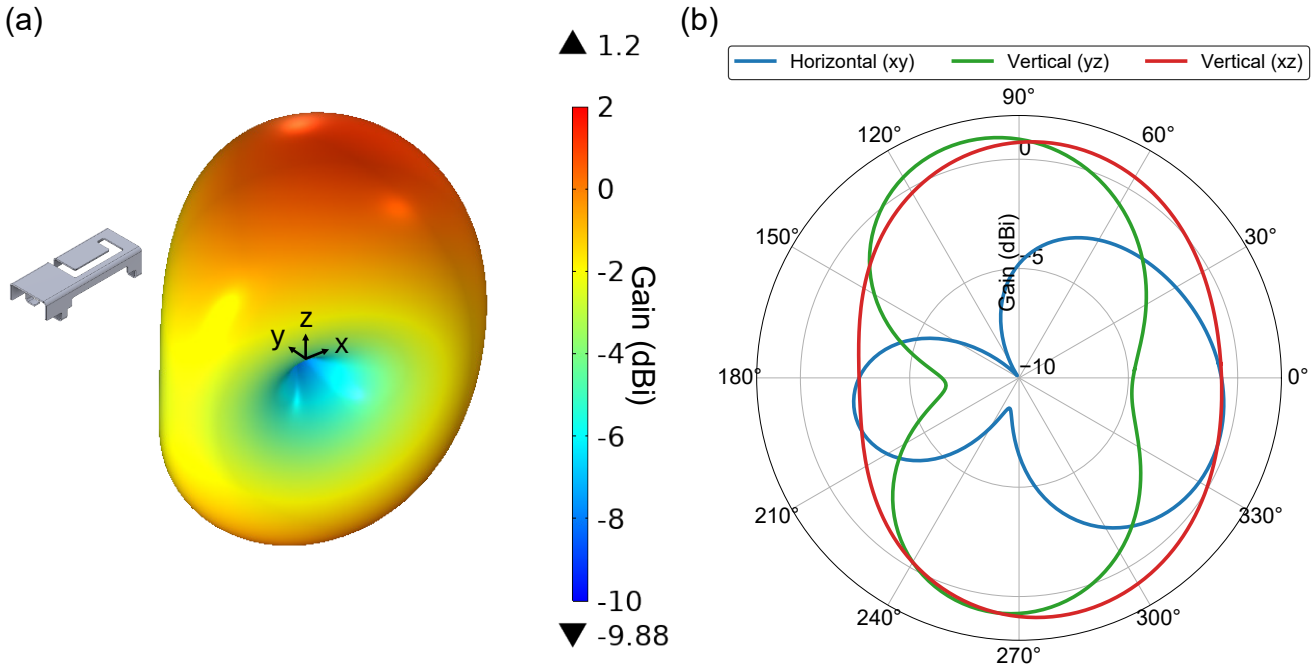

Figure S9. Simulated radiation pattern of the 3D metal antenna on the PCB at 2.45 GHz. (a) 3D gain pattern. (b) 2D gain patterns in the horizontal (xy) and vertical (yz, xz) planes.

Fluoxetine concentration

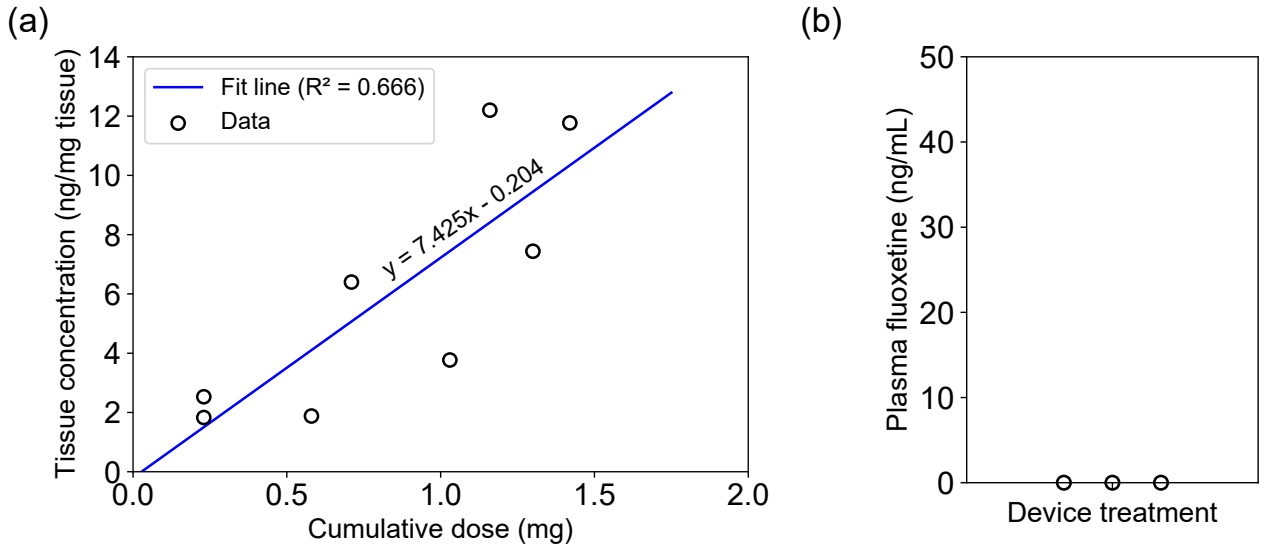

Figure S10. (a) The wound tissue concentration of fluoxetine was strongly correlated with the cumulative dose delivered by the experimental device (Spearman's r = 0.862, p = 0.005873, from n = 8 wounds treated with Flx^{+} devices from 3 independent experiments). The cumulative dose represents the total amount of fluoxetine delivered to each wound by the device over the course of the 7-day treatment. (b) Fluoxetine was not detectable in pig plasma (n = 3 pigs) following topical fluoxetine wound treatment using the experimental device.

PDMS fabrication

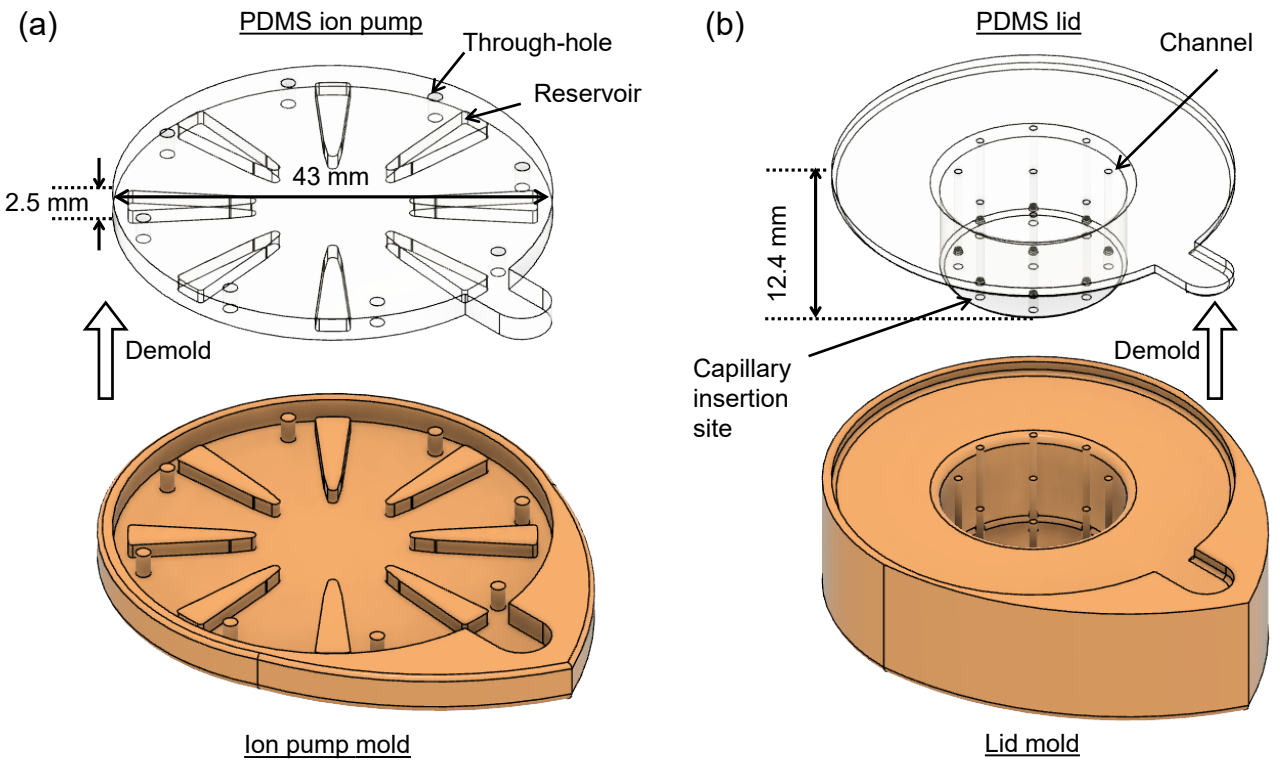

Figure S11. Fabrication process of the PDMS device using 3D-printed two-part molds. Created with Autodesk Fusion 2024 and annotated in Microsoft PowerPoint 2025. (a) PDMS ion pump and its mold. (b) PDMS lid and its mold.